



A parameter-free dynamic subgrid-scale model for large-eddy simulation

Andrés E. Tejada-Martínez¹, Kenneth E. Jansen^{*}

*Scientific Computation Research Center and Mechanical, Aerospace & Nuclear Engineering,
Rensselaer Polytechnic Institute, Troy, NY 12180-3590, USA*

Received 15 March 2004; received in revised form 10 September 2004; accepted 19 September 2004

Abstract

We present a new dynamic Smagorinsky subgrid-scale model in which the sole model parameter, the filter width ratio, is computed dynamically. The resulting expression for the filter width ratio is parameter-free, as difficult-to-compute filter widths required in earlier models are no longer necessary. Traditionally, the filter width ratio is taken as a constant based on assumptions which do not hold in general for all numerical discretizations. Previous work has shown that simulation results may strongly depend on the filter width ratio parameter, thus motivating its accurate determination. The new dynamic model is tested on large-eddy simulation of decaying isotropic turbulence on hexahedral, tetrahedral, and wedge topologies using the stabilized finite element method developed by Whiting and Jansen [C.H. Whiting, K.E. Jansen, A stabilized finite element method for the incompressible Navier–Stokes equations using a hierarchical basis, *Int. J. Numer. Methods Fluids* 35 (2001) 93–116].

© 2005 Elsevier B.V. All rights reserved.

1. Introduction

Recently, in [16] the authors developed a procedure for dynamic estimation of the filter width ratio, the model parameter appearing in the dynamic Smagorinsky model for large-eddy simulation (LES) of turbulent flows. The model parameter is a ratio involving the width of the primary filter used for deriving the filtered Navier–Stokes equations and the width of the compound filter resulting from sequential applications of the primary and a test filter. The test filter is used as part of a procedure to obtain the model coefficient dynamically (see [2,6]). As discussed by the authors in [16], there is an ambiguity in setting the model

^{*} Corresponding author. Tel.: +1 518 2766755; fax: +1 518 2766025.

E-mail address: kjansen@scorec.rpi.edu (K.E. Jansen).

¹ Present address: Center for Coastal Physical Oceanography, Old Dominion University, Norfolk, VA, USA.

parameter stemming from the fact that the primary filter (or grid filter) is inherently applied by the discretization. Consequently, there is no possibility of determining the shape and thereby the width of the primary filter, let alone the shape and width of the compound filter resulting from the primary and test filters.

To bypass this ambiguity, if the discretization involves finite differences, the grid filter is often assumed to be twice the characteristic size of the grid, such as

$$\bar{\Delta} = 2(h_1 h_2 h_3)^{1/3} \quad \text{or} \quad \bar{\Delta} = 2(h_1^2 + h_2^2 + h_3^2)^{1/2}, \quad (1)$$

where h_i is the grid spacing in the i th direction. There exists an equivalence between the exact derivative of a filtered variable and the central difference derivative of the unfiltered variable (see [7,12,17]), leading to the conclusion that the implicit grid filter behaves like the well-known box filter of width twice the grid size. In brief, after choosing the test filter and assuming a specific form for the grid filter, the filter width ratio can be computed (see [19]). Furthermore, if the discretization involves a spectral method, the grid filter can be assumed to be the sharp cutoff spectral filter and its width can be easily computed from well-known definitions given in [10]. However, in general an assumption regarding the form of the grid filter cannot be made, leaving one to estimate its width.

To demonstrate the effect of the implicit filter associated to the discretization, we direct the reader to Fig. 1. In this figure we present LES results of infinite Reynolds number isotropic turbulence. The turbulence decays in time due to the action of the subgrid-scale stress in the absence of an energy source. The energy spectrum of the initial condition is purposely set so that it behaves as $k^{-5/3}$ near and at the cutoff wavenumber. Even though the turbulence is decaying, the energy spectrum of the solution at later times should ideally preserve the $k^{-5/3}$ behavior near and at the cutoff wavenumber. The energy spectrum of the solution was collected at two instances to see if the spectra followed the $k^{-5/3}$ behavior at the cutoff wavenumber. The $k^{-5/3}$ behavior is preserved in the approximate range of $7 < k < 10$, however, as expected, the spectrum at and near the cutoff wavenumber, in this case $k = 16$, is damped by the implicit filter associated to the discretization. Note that this damping of scales at the highest wavenumbers occurs regardless of the subgrid-scale model used and only depends on the discretization. The discretization used for the results in Fig. 1 employs the stabilized finite element developed in [14,18]. The implicit filtering characteristic of stabilized methods such as this one (tending to damp the smallest resolved scales) has also been observed

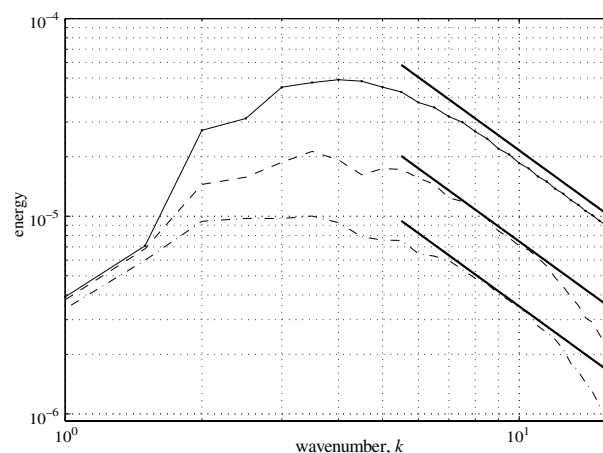


Fig. 1. Spectra of infinite Reynolds number decaying isotropic turbulence in a cube of sides of length 2π with 33 points in x , y and z . The grid was composed of hexahedral elements. (—●—): spectrum of initial condition; (---): spectrum of solution at $t = 56$; (-·-·-): spectrum at $t = 129$; (—): $-5/3$ slope.

by other researchers as described in [3]. If the discretization were to have employed a spectral method, then the high wavenumber damping would not have occurred and any difference between the resulting energy spectra and a $k^{-5/3}$ behavior at the highest wavenumbers would be attributable to the model. Given the unavoidable damping of resolved scales at high wavenumbers by the implicit filter associated to numerical methods in general, we focus on accurately representing scales larger than those affected by the method's implicit filter. As will be shown later, the representation of scales larger than those affected by the method's implicit filter can be sensitive to the dynamic model parameter, thus motivating the need for accurate determination of the model parameter. This sensitivity issue deserves special attention especially for cases where LES grids are coarsened, leading to larger subgrid-scale model contributions.

The authors have presented a method in [16] in which a dynamic expression for the model parameter is derived through the application of a second test filter. The method is based on the fact that dynamic model results can be independent of the test filter if the width of the test filter is consistently computed, a result shown by Lund in [7] and the authors in [15,16]. In other words, the Smagorinsky coefficient as rendered by the dynamic model, depends solely on the discretization and not on the test filter. The only parameter required in the derivation of the dynamic expression for the model parameter, herein referred to as DFWR1, is the ratio between the widths of the first and second test filters. Both filters are explicitly applied, thus their widths can be computed. DFWR1 essentially samples the resolved field and inherently extracts information regarding the grid filter width.

Several test filters have been proposed in [16] for which transfer functions can be computed and used to define filter widths. These test filter widths are required by DFWR1 to dynamically compute the model parameter. However, with the advent of complex geometry dynamic model LES (see [5]), obtaining transfer functions for filters defined on such geometries can prove to be cumbersome and expensive. Filters on complex geometries can be well-defined, such as in [8], however, determination of their widths can require extensive pre-processing computations, especially if the test filter shape is changing throughout the mesh. Thus, determining test filter widths required as inputs to DFWR1 and to the classic model as well, can prove to be difficult. Further complicating matters, results may have a strong dependence on the model parameter, thus requiring its accurate computation. Therefore, the objective of the current work is to derive and test a generalized version of DFWR1 (herein referred to as DFWR2) with the intent of eliminating the need for test filter widths, required by DFWR1 and earlier models, resulting in a parameter-free dynamic Smagorinsky model. Furthermore, DFWR2 will be shown to be general enough that the scale-invariance assumption (reviewed in [9]) made in the classic dynamic model is not required as the resulting parameter-free model can be considered scale-dependent, similar to the model of Porté-Agel et al. in [11]. Although the scale-dependency of DFWR2 is not tested here, it should be pursued in future investigations.

2. The classic dynamic model

Application of an arbitrary homogeneous spatial filter (with kernel $G_{\bar{\Delta}}$ and width $\bar{\Delta}$) to the Navier–Stokes equations yields the following residual stress tensor, often referred to as the subgrid-scale stress:

$$\tau_{ij} = \overline{u_i u_j} - \bar{u}_i \bar{u}_j. \quad (2)$$

The bar symbol ($\bar{\cdot}$) denotes application of the homogeneous spatial filter. The negative of the divergence of the subgrid-scale stress tensor appears on the right hand side of the filtered equations. Note that application of the spatial filter previously mentioned (herein referred to as the primary filter) is implicit because the filtered Navier–Stokes equations are solved for the filtered velocity \bar{u}_i in the presence of a model for the subgrid-scale stress. The role of the primary filter is assumed by the numerical discretization, which is why it is often referred to as the grid filter.

In the dynamic subgrid-scale model, the coefficient present in the Smagorinsky model (first proposed in [13]) is dynamically computed with the aid of the Germano identity, developed in [2]. This identity considers the stresses at the $G_{\bar{\Delta}}$ -level, given in (2), and at the $G_{\hat{\Delta}}$ -level, where $G_{\hat{\Delta}}$ is the filter kernel (of width $\hat{\Delta}$) resulting from sequential application of the grid filter and a test filter. Filtering with the compound filter kernel $G_{\bar{\Delta}}$ is denoted by $(\bar{\cdot})$, and filtering with the test filter kernel $G_{\hat{\Delta}}$ alone is denoted by $(\hat{\cdot})$. The Germano identity takes the form

$$L_{ij} = T_{ij} - \hat{\tau}_{ij}, \quad (3)$$

where T_{ij} , defined as

$$T_{ij} = \widehat{u_i u_j} - \hat{u}_i \hat{u}_j \quad (4)$$

is the residual stress generated after the Navier–Stokes equations are filtered with the compound filter of kernel $G_{\bar{\Delta}}$; T_{ij} is the stress at the $G_{\bar{\Delta}}$ -level. The tensor L_{ij} in (3) can be expressed in terms of resolved and modeled quantities. In terms of the former, L_{ij} becomes

$$L_{ij} = \widehat{u_i u_j} - \hat{u}_i \hat{u}_j. \quad (5)$$

L_{ij} is obtained in terms of modeled quantities after the deviatoric portions of residual stresses τ_{ij} and T_{ij} are expressed through the Smagorinsky model as

$$\tau_{ij}^d \equiv \tau_{ij} - \frac{1}{3} \tau_{kk} \delta_{ij} = -2(C_s^{\bar{\Delta}} \bar{\Delta})^2 |\bar{S}| \bar{S}_{ij} \quad (6)$$

and

$$T_{ij}^d \equiv T_{ij} - \frac{1}{3} T_{kk} \delta_{ij} = -2(C_s^{\hat{\Delta}} \hat{\Delta})^2 |\hat{S}| \hat{S}_{ij}, \quad (7)$$

where

$$\bar{S}_{ij} = \frac{1}{2} \left(\frac{\partial \bar{u}_i}{\partial x_j} + \frac{\partial \bar{u}_j}{\partial x_i} \right), \quad |\bar{S}| = (2\bar{S}_{ij} \bar{S}_{ij})^{1/2}, \quad (8)$$

$$\hat{S}_{ij} = \frac{1}{2} \left(\frac{\partial \hat{u}_i}{\partial x_j} + \frac{\partial \hat{u}_j}{\partial x_i} \right), \quad \text{and} \quad |\hat{S}| = (2\hat{S}_{ij} \hat{S}_{ij})^{1/2}. \quad (9)$$

Furthermore, $C_s^{\hat{\Delta}}$ and $C_s^{\bar{\Delta}}$ are the Smagorinsky coefficients corresponding to the modeled stress at the $G_{\hat{\Delta}}$ -level and the modeled stress at the $G_{\bar{\Delta}}$ -level, respectively. Under the assumption of scale-invariance, $C_s^{\hat{\Delta}} = C_s^{\bar{\Delta}} = C_s$ can be taken. A least squares minimization of the difference between the modeled and resolved expressions for the deviatoric portion of L_{ij} with respect to C_s yields the following expression for the model coefficient:

$$(C_s \bar{\Delta})^2 = \frac{1}{2} \frac{\langle L_{ij} M_{ij} \rangle}{\langle M_{kl} M_{kl} \rangle}, \quad (10)$$

where L_{ij} is given by (5) and

$$M_{ij} = |\bar{S}| \bar{S}_{ij} - \alpha |\hat{S}| \hat{S}_{ij}. \quad (11)$$

Accurate estimation of the squared filter width ratio given as $\alpha = (\hat{\Delta}/\bar{\Delta})^2$ is the main focus here. The brackets in (10) denote spatial averaging over homogeneous directions of the flow.

2.1. Test filters

Given that the discretization of choice is the Streamline Upwind/Petrov–Galerkin (SUPG) finite element method (see [14,18]), test filters on finite element topologies, analyzed in [16,15], will be used. Numerical integration based on Gaussian quadrature can be used to approximate a filtered function leading to several discrete forms. For example, a one-dimensional box filtered function at $x = x_0$ approximated with the one-point Gaussian quadrature rule leads to

$$\int G(x_0, y)f(y) dy = \int_{x_{-1}}^{x_1} f(y) dy \approx \frac{1}{2}(f_{-1/2} + f_{1/2}) = \hat{f}_0, \quad (S1) \tag{12}$$

where $f_0 = f(x_0)$, $f_{-1/2} = f(x_{-1/2})$, and $f_{1/2} = f(x_{1/2})$. $x = x_{1/2}$ and $x = x_{-1/2}$ mark the locations of the quadrature points symmetrically situated about $x = x_0$, as seen in Fig. 2. The box filter is the local average of the function $f(x)$ about $x = x_0$, extending to adjacent vertices at $x = x_{-1}$ and $x = x_1$. Here, the box filter kernel, G , takes on the constant value $1/(2h)$ in the interval (x_{-1}, x_1) and 0 elsewhere. The discrete form in (12) will be referred to as filter S1, which stands for standard filter evaluated with one-point quadrature. If the filtered function \hat{f}_0 is assumed piecewise linear and is filtered once again with the box filter, and if such operation is approximated with one-point quadrature, we obtain

$$\tilde{f}_0 = \frac{1}{8}f_{-3/2} + \frac{3}{8}f_{-1/2} + \frac{3}{8}f_{1/2} + \frac{1}{8}f_{3/2}, \quad (W1) \tag{13}$$

where W1 is short notation for wide filter using one-point Gaussian quadrature. Filter W1 is said to be wider than filter S1 since it attenuates scales larger than those attenuated by S1. The reader is directed to Fig. 2 for locations of function evaluations $f_{\pm m/n}$ (i.e. quadrature point locations corresponding to one-point Gaussian quadrature).

Different versions of filters S1 and W1 can be obtained if the first filter operation is carried out using two-point Gaussian quadrature. In that case, we obtain

$$\hat{f}_0 = \frac{1}{4}(f_{-2/3} + f_{-1/3} + f_{1/3} + f_{2/3}), \quad (S2) \tag{14}$$

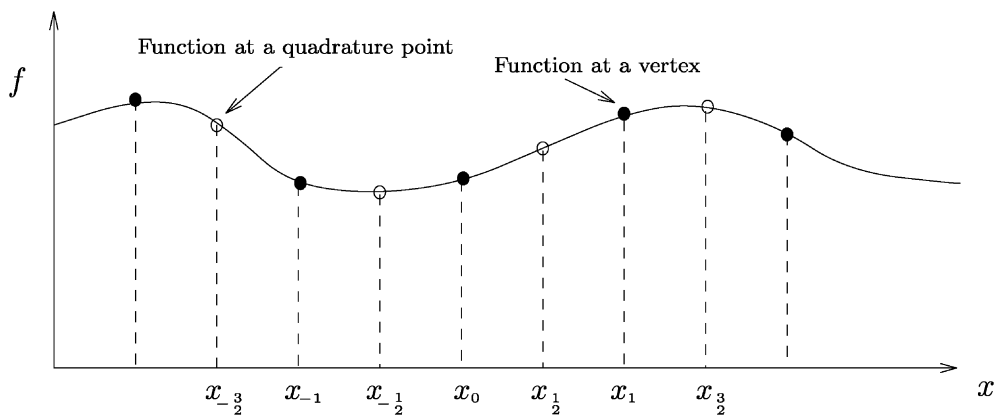


Fig. 2. Sketch of function evaluations for filters S1 and W1. Each quadrature point is located at the middle of an element (the interval between two vertices). The spacing between vertices is h .

and

$$\tilde{f}_0 = \frac{1}{16}(f_{-5/3} + f_{-4/3}) + \frac{3}{16}(f_{-2/3} + f_{-1/3}) + \frac{3}{16}(f_{1/3} + f_{2/3}) + \frac{1}{16}(f_{4/3} + f_{5/3}), \quad (\text{W2}) \quad (15)$$

$f_{\pm m/n}$ denote the function $f(x)$ evaluated at specific quadrature point locations, relative to $x = x_0$. These quadrature point locations, corresponding to two-point quadrature, can be found in [4].

Discrete kernels associated to filters S and W in (12)–(15) may be expressed as

$$G(r) = \sum_{i=-J}^J W_i \delta(r + \lambda_i), \quad (16)$$

where δ is the Dirac delta function, $2J$ is the number of function evaluations, W_i ($W_0 = 0$) are the weights of the function evaluations, and λ_i (for $i = -J, \dots, -1, 1, \dots, J$) define the function evaluation locations (i.e. quadrature point locations). In the case of filter S1, $J = 1$, $W_{\pm 1} = 1/2$, and $\lambda_{\pm 1} = x_{\pm 1/2} = \pm h/2$.

The Fourier transform (multiplied by 2π) of the discrete kernel in (16) is defined as the filter transfer function. For regularly connected grids possessing quadrature points located symmetrically about $x = x_0$ (i.e. $x_{m/n} = -x_{-m/n}$ hence $\lambda_i = -\lambda_{-i}$) the resulting transfer function is real and may be written as

$$\mathcal{G}(k) = 2 \sum_{i=1}^J W_i \cos(k\lambda_i). \quad (17)$$

The filter width may be computed as $\Delta = \pi/k^*$, where k^* is obtained as the wavenumber corresponding to a specified value (usually ≥ 0.5) of $\mathcal{G}(k)$. A second definition of the filter width may be taken based on the second moment of the filter kernel as

$$\Delta = \left(12 \int_{-\infty}^{\infty} r^2 G(r) dr \right)^{1/2}. \quad (18)$$

Note that evaluating the previous expression with $G(r)$ given by a box filter with non-vanishing kernel over a length of say L results in $\Delta = L$, precisely the defined width of the box filter. Inserting (16) into (18) results in

$$\hat{\Delta} = \left(12 \sum_{i=-J}^J W_i \lambda_i^2 \right)^{1/2}. \quad (19)$$

The previous filter width definition is convenient for filters on hexahedral grids, where multi-dimensional filters can be constructed from sequential applications of one-dimensional filters. However, this is not the case for filters on multi-dimensional topologies such as tetrahedral or wedge topologies. The filter width definition based on the transfer function can be easily generalized for multiple dimensions, and thus is more practical.

Following the same steps previously outlined, filters S and W can be constructed on two-dimensional and three-dimensional grids. Any finite element-based (quadrature-based) test filtered function (with test filter S1, S2, W1, or W2) at vertex location $\mathbf{x} = \mathbf{x}_0$ on two- or three-dimensional regularly connected topologies takes the form

$$\hat{f}(\mathbf{x}_0) = \sum_{i=-J}^J W_i f(\mathbf{x}_i), \quad (20)$$

where the \mathbf{x}_i (for $i = -J, \dots, -1, 1, \dots, J$) denote quadrature point locations symmetrically located about vertex \mathbf{x}_0 . For example, consider test filtering a function on the regularly connected triangular and quadri-

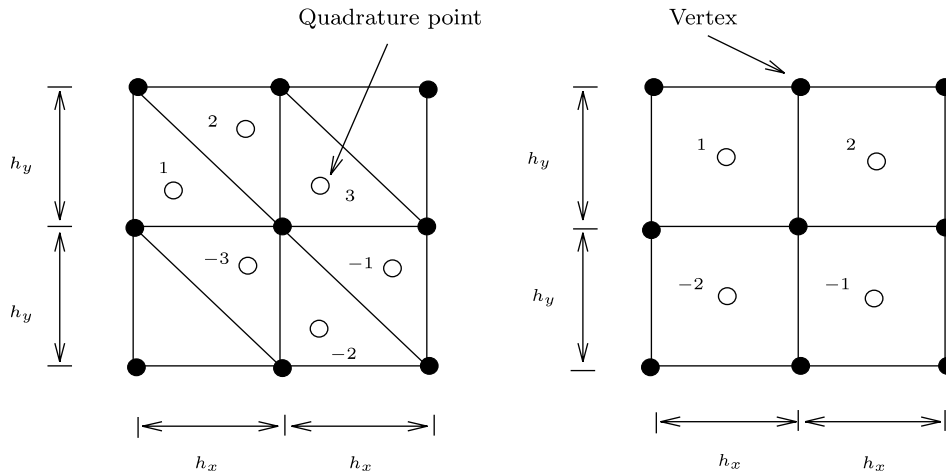


Fig. 3. Sketch of regularly connected triangular and rectangular grids. Each quadrature point is located at the centroid of its element. Quadrature point locations are symmetric ($x_i = -x_{-i}$) with respect to the middle vertex, x_0 .

lateral grids shown in Fig. 3 using one-point quadrature. Given the symmetry of the quadrature points about the middle vertex, x_0 , the transfer functions of the filters are real and can be used to define filter widths in the same fashion described before for the one-dimensional cases.

Several examples of three dimensional constructions of quadrature-based (finite element-based) filters on regularly connected hexahedral, tetrahedral and wedge grids are provided in [16]. However, writing explicit expressions for the three-dimensional filters S and W is impractical because of the infinite number of possibilities that might arise if using irregular connections and because of the large number of function evaluations involved. For example, in the case of filter S1 on hexes there are 8 function evaluations corresponding to the single quadrature point in each element of the group of 8 elements sharing the vertex at which the filtered function is desired; for filter S2 on hexes there are 64 function evaluations because there are 8 quadrature points in each element sharing the desired vertex.

In general, real transfer functions for filters S and W applied on regularly connected hexahedral, tetrahedral and wedge topologies can be computed thanks to the symmetry of the quadrature point locations discussed earlier. Furthermore, isosurfaces of these transfer functions defined by an arbitrary value of the transfer function can be used to compute filter widths. More precisely, an average radial wavenumber ($k_r^* = \sqrt{k_x^{*2} + k_y^{*2} + k_z^{*2}}$) associated to the specified isosurface may be extracted and used to define the filter width in the same way described earlier (i.e. $\Delta = \pi/k_r^*$). For example, the squared widths of filters S1 and S2 on a hexahedral grid with constant spacing h based on the transfer function isosurface defined by 0.75 is $(\hat{\Delta}/h)^2 = 7.36$ and $(\hat{\Delta}/h)^2 = 9.57$, respectively. For filters W1 and W2, the widths are $(\hat{\Delta}/h)^2 = 21.1$ and $(\hat{\Delta}/h)^2 = 23.4$, respectively. The interested reader is directed to [16] for details. Thus, filter W1 is about 2.9 times wider than filter S1, and filter W2 is about 2.4 times wider than filter S2. Different isosurfaces yield different widths, however, the relative width of filters on hexahedral (hex), tetrahedral (tet), or wedge topologies remains the same, as is shown in [16]. In other words, the relative width between filters S1 (viz. S2) and W1 (viz. W2) on a given topology remains the same across isosurfaces. This property of our test filters allows DFWR1 results to be independent of the chosen isosurface, as the only input parameter is the ratio between the widths of the standard and wide test filter used. The new model introduced here (which we will refer to as DFWR2) eliminates the need to compute filter transfer functions and filter widths, a task which is extremely cumbersome even on the regularly connected topologies considered here.

3. Dynamic estimation of the filter width ratio

3.1. The classic dynamic model with standard and wide test filters

In this sub-section, we test the classic dynamic model with the standard and wide test filters and show the strong effect that the filter width ratio parameter can have on results. Furthermore, we will demonstrate that the classical dynamic model can lead to nearly identical results independent of the test filter used as long as the test filter width is consistently computed following a single definition. For this we perform LES of decaying isotropic turbulence in a periodic cube with sides 2π in length, discretized by a relatively coarse grid with 33 vertices in each direction spaced at a constant length $h = 2\pi/32$.

The grid is split by hexahedral elements, although in upcoming sub-sections cases for which the same grid is split by regularly connected tetrahedral and wedge elements will be considered as well. The initial conditions were obtained based on experimental data presented in [1] at a non-dimensional time station denoted as t_{42} . This problem is homogeneous in the x -, y -, and z -directions, thus spatial averaging of the dynamic model's numerator and denominator is performed over these three directions.

First, let us review how the classic dynamic model takes form under the standard and wide test filters and without the scale-invariance assumption. We will be working with residual stresses at three levels. These stresses include the usual ones at the subgrid-level (or the G_{Δ} -level) and at the subtest level (or the $G_{\tilde{\Delta}}$ -level):

$$\tau_{ij} = \overline{u_i u_j} - \bar{u}_i \bar{u}_j \quad (21)$$

and

$$T_{ij} = \widehat{u_i u_j} - \hat{u}_i \hat{u}_j, \quad (22)$$

respectively. In addition, we consider the stress at a secondary subtest level (or the $G_{\tilde{\tilde{\Delta}}}$ -level):

$$\mathcal{T}_{ij} = \widetilde{\widehat{u_i u_j}} - \widetilde{\hat{u}_i \hat{u}_j}. \quad (23)$$

The previous stress is obtained when the Navier–Stokes equations are filtered thrice using the grid filter, followed by the test filter and a second test filter. This operation is denoted by $(\widetilde{\cdot})$. Application of the second test filter alone is denoted by $(\widehat{\cdot})$, and sequential application of the two test filters is denoted by $(\widehat{\widehat{\cdot}})$. The compound filter resulting from the sequential application of the test filters is what we call the wide filter, as discussed in Section 2.1. Once again, the reader is reminded that application of the grid filter $(\bar{\cdot})$ does not appear explicitly and is assumed by the discretization, unlike application of the two test filters.

Following the dynamic procedure described in the previous section, but this time without making the scale-invariance assumption, leads to

$$(C_s^{\tilde{\Delta}} \tilde{\Delta})_{\text{std}}^2 = \frac{1}{2} \frac{\langle L_{ij} M_{ij} \rangle}{\langle M_{kl} M_{kl} \rangle} \equiv \Theta_1(\alpha \zeta), \quad (24)$$

where L_{ij} is given in (5) and now M_{ij} becomes

$$M_{ij} = |\widehat{\widehat{S}}| \widehat{\widehat{S}}_{ij} - \alpha \zeta |\widehat{\widehat{S}}| \widehat{\widehat{S}}_{ij}. \quad (25)$$

Parameter $\alpha = (\tilde{\Delta}/\tilde{\tilde{\Delta}})^2$ is the square of the filter width ratio as before, and $\zeta = (C_s^{\tilde{\tilde{\Delta}}}/C_s^{\tilde{\Delta}})^2$ involves the ratio between the Smagorinsky coefficients at the $G_{\tilde{\tilde{\Delta}}}$ -level and the $G_{\tilde{\Delta}}$ -level. The subscript “std” refers to the hat notation, $(\widehat{\cdot})$, as potential application of one of the standard filters (S1 or S2) in (12) and (14).

Analogous to (6) and (7), the stress in (23) can be modeled as

$$\mathcal{T}_{ij}^d = -2(C_s^{\tilde{\tilde{\Delta}}} \tilde{\tilde{\Delta}})^2 |\widetilde{\widehat{\widehat{S}}}| \widetilde{\widehat{\widehat{S}}}_{ij}. \quad (26)$$

Least squares minimization of the difference between the modeled and resolved expressions for the Germano identity between the $G_{\bar{\Delta}}$ -level and the $G_{\hat{\Delta}}$ -level yields

$$(C_s^{\bar{\Delta}}\bar{\Delta})_{\text{wide}}^2 = \frac{1}{2} \frac{\langle \mathcal{L}_{ij}\mathcal{M}_{ij} \rangle}{\langle \mathcal{M}_{kl}\mathcal{M}_{kl} \rangle} \equiv \Theta_2(\beta\eta), \tag{27}$$

where

$$\mathcal{L}_{ij} = \widetilde{\widetilde{u_i u_j}} - \widetilde{\widetilde{u_i}}\widetilde{\widetilde{u_j}}, \tag{28}$$

$$\mathcal{M}_{ij} = |\widetilde{\widetilde{S}}|_{ij} - \beta\eta|\widetilde{\widetilde{S}}|_{ij}, \tag{29}$$

$\beta = (\hat{\Delta}/\bar{\Delta})^2$, and $\eta = (C_s^{\hat{\Delta}}/C_s^{\bar{\Delta}})^2$. The subscript “wide” refers to the tilde-hat notation, $(\hat{\cdot})$, as potential application of one of the wide filters (W1 or W2) in (13) and (15). The expressions in (24) and (27) give the dynamic model coefficient without the scale-invariance assumption with standard and wide test filters, respectively.

For the moment, let us assume scale-invariance (as is done in the classic dynamic model), thus $\zeta = 1$ and $\eta = 1$ (i.e. $C_s^{\bar{\Delta}} = C_s^{\hat{\Delta}} = C_s^{\widetilde{\hat{\Delta}}} = C_s$), and let us hypothesize that α and β , appearing in (25) and (29), can be taken as

$$\alpha \equiv \left(\frac{\hat{\Delta}}{\bar{\Delta}}\right)^2 = \kappa \left(\frac{\hat{\Delta}}{h}\right)^2 \tag{30}$$

and

$$\beta \equiv \left(\frac{\widetilde{\hat{\Delta}}}{\bar{\Delta}}\right)^2 = \kappa \left(\frac{\widetilde{\hat{\Delta}}}{h}\right)^2, \tag{31}$$

where κ is a tuning parameter representing the dependence of the filter width ratio on the grid filter width, $\bar{\Delta}$. Notice that in the classic dynamic model with either a standard or wide test filter, an assumption such as in (30) or in (31) is required, specifically because the shape and thus the width of the implicit grid filter is not known. Under the assumptions in (30) and (31), the model coefficients in (24) and (27) give nearly identical results, as long as test filter widths, $(\hat{\Delta}/h)$ and $(\widetilde{\hat{\Delta}}/h)$, are computed consistently using a specified definition (see [16]). For example, tracking the temporal behavior of model coefficients given by (24) and (27) in our simulations of decaying isotropic turbulence, we can see that model coefficient ratios, $(C_s^{\bar{\Delta}})_{\text{std}}/(C_s^{\bar{\Delta}})_{\text{wide}}$, are nearly one, as is shown in Fig. 4. From this we conclude that the classic dynamic model produces nearly identical model coefficients regardless of the filter used, leading to nearly indistinguishable results in terms of energy spectra seen in Fig. 5. In Fig. 5, we compare energy spectra resulting from dynamic model simulations using different standard and wide test filters. Energy spectra corresponding to the different test filters are nearly identical. The energy spectrum of the initial condition in each simulation (not shown in Fig. 5) was set to match the experimental energy spectrum of [1] at an initial non-dimensional time station, t_{42} . Simulations ran up to t_{98} at which point energy spectra of the solution were collected.

Although simulation results can be independent of the test filter employed in the dynamic model (either a standard or wide test filter), these results may not be optimal (as demonstrated by Fig. 5 with respect to experimental data at t_{98}) unless the correct value of the tuning parameter κ and thus the correct value of the filter width ratio are known. An accurate value of the filter width ratio is important for coarse grid simulations, as results tend to strongly depend on this parameter. In Fig. 6, we show the effect of changing the filter width ratio in our dynamic model results of decaying isotropic turbulence while using standard filter S1 on hexes. Here we compare energy spectra obtained with different values of the filter width ratio to the experimental energy spectra data recorded in [1] at non-dimensional time stations t_{98} and t_{171} . The energy

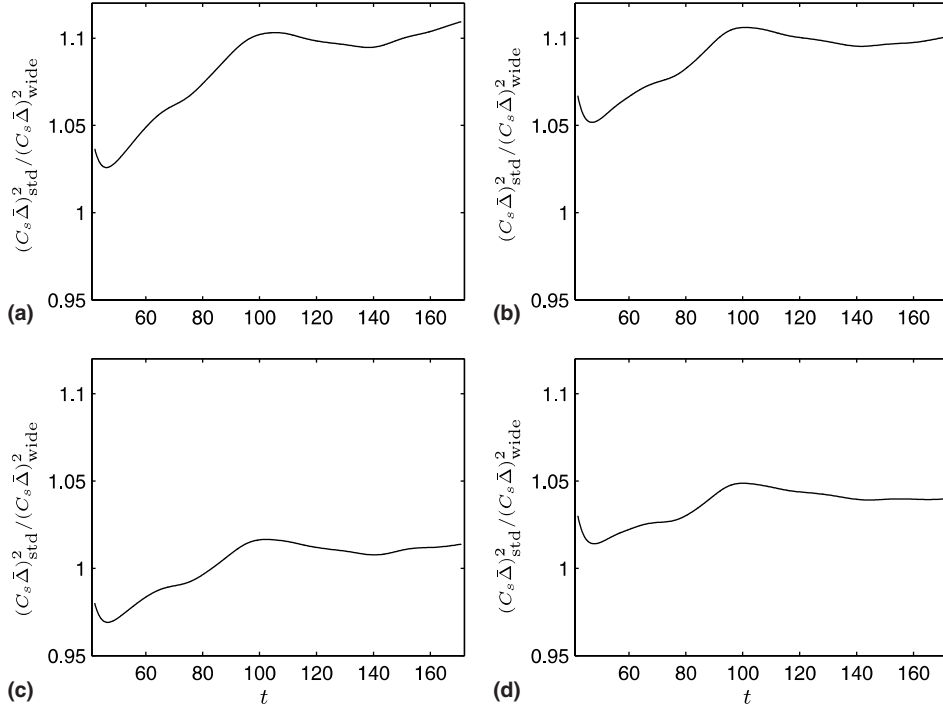


Fig. 4. Ratio between dynamic model coefficients in decaying isotropic turbulence obtained using the classic dynamic model with standard and wide filters. Assumption (30) and (31) were made and test filter widths were set as suggested in Section 2.1. For example in (a), in the case of standard filter S1, $\alpha = \kappa(\hat{\Delta}/h)^2 = 0.680(7.36) = 5.00$ and in the case of wide filter W1, $\beta = \kappa(\hat{\Delta}/h)^2 = 0.680(21.1) = 14.3$. (a) Simulations with S1 and W1 and $\kappa = 0.680$, (b) simulations with S2 and W2 and $\kappa = 0.680$, (c) simulations with S1 and W1 and $\kappa = 0.544$, and (d) simulations with S1 and W2 and $\kappa = 0.544$.

spectrum of the initial condition in each simulation matching the experimental energy spectrum of [1] at t_{42} is shown as well. Notice the strong effect of this parameter on the energy spectrum in the inertial range (i.e. wavenumbers between 3 and 8 in this case), thus its accurate prediction is of primary importance. Furthermore, the simulations with $\alpha = 2$ and $\alpha = 3$ have been extended to t_{171} , while the others were stopped at t_{98} . The $\alpha = 3$ simulation uses the customary estimate $\alpha \approx (\hat{\Delta}/h)^2 = 3$, which is based on the assumption in (30) where $\kappa = 1$ has been taken and where the test filter width $\hat{\Delta}$ has been computed based on the second moment of the test filter kernel used (filter S1), as described earlier and in [15] and [7]. Clearly, this simulation shows that for our stabilized finite element method such an estimate of α is not appropriate as it leads to an over-prediction of energy at t_{98} and t_{171} . A second customary estimate is to take $\bar{\Delta} \approx h$ and $\hat{\Delta}^2 \approx \bar{\Delta}^2 + h^2$, where h is the grid size. In this case, $\alpha \approx (\hat{\Delta}^2 + h^2)/h^2 = 4$. However, similar to $\alpha \approx 3$, the estimate $\alpha \approx 4$ leads to an over-prediction of energy at t_{98} . At first sight, the simulation with $\alpha = 2$ might seem optimal as it is a best fit of the t_{98} experimental spectrum extending through the highest resolved wavenumbers. However, the reader is reminded that in an LES we aim at good agreement in the inertial range prior to the highest resolved wavenumbers, as the latter scales are strongly affected by numerical error. It is commonly understood that low order methods, such as ours, are not able to represent spectra up to the highest resolved wavenumbers, unlike spectral methods. Looking closely at Fig. 6, we see that at t_{98} the $\alpha = 2$ case does not give optimal results because the energy in the inertial range is slightly over-predicted. In this case, the model coefficient $(C_s \hat{\Delta})^2$ is slightly low, and fortuitously, the energy spectra at the high resolved wavenumbers matches the data at t_{98} . However, this no longer occurs at t_{171} .

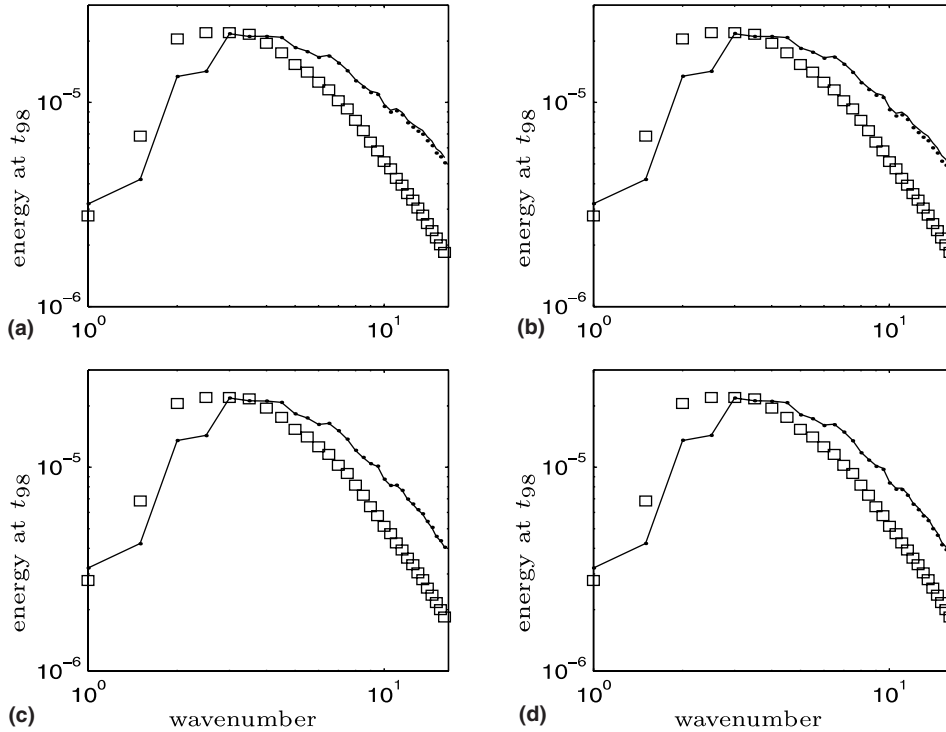


Fig. 5. Simulations of isotropic turbulence on hexes comparing dynamic model results with different test filters. (a) Two simulations, one with filter S1, the other with filter W1, and both with $\kappa = 0.680$. (b) Two simulations, one with filter S2, the other with filter W2, and both with $\kappa = 0.680$. (c) Two simulations, one with filter S1, the other with filter W1, and both with $\kappa = 0.544$. (d) Two simulations, one with filter S2, the other with filter W2, and both with $\kappa = 0.544$. For all plots, (—): standard filter S1 or S2; (●): wide filter W1 or W2; (□): data at t_{98} .

3.2. The parameter-free model

Recall the full expressions for the model coefficient based on a standard filter in (24) or on a wide filter in (27) without invoking scale-invariance nor assuming a form for the filter width ratio squared such as (30) or (31). Looking at (24) and (27), we have two unknowns, namely $\xi_1 = \alpha\zeta$ and $\xi_2 = \beta\eta$. Results of the previous section, shown in Fig. 4, motivate equating (24) and (27) thus giving us the first equation for the two unknowns ($\xi_1 = \alpha\zeta$ and $\xi_2 = \beta\eta$):

$$\Theta_1(\xi_1) = \Theta_2(\xi_2). \tag{32}$$

Porté-Angel et al. [11], arrive at the same expression, except that they set their squared filter width ratios as $\alpha = 2^2$ and $\beta = 4^2$ and use different test filters as the ones described here. Their motivation is obtaining a scale-dependent model (such that $C_s^\Delta \neq C_s^\Delta$) and not obtaining a dynamic filter width ratio expression. The expression used here is more general given that in addition to being scale-dependent, it does not assume any values for the filter width ratios. Furthermore, even after setting the filter width ratios, α and β , expression (32) still has two unknowns, namely $\xi_1 = \zeta$ and $\xi_2 = \eta$. To that extent, Porté-Angel et al. assume a power law behavior for C_s^Δ , which leads them to the form $\eta = \zeta^2$. Instead, here we will obtain a second scale-dependent equation that coupled with Eq. (32) can be used to solve for the pair of unknowns $\xi_1 = \alpha\zeta$ and $\xi_2 = \beta\eta$, without the need to assume a power law behavior for the Smagorinsky coefficient nor a behavior for the squared filter width ratio such as in (30) and (31).

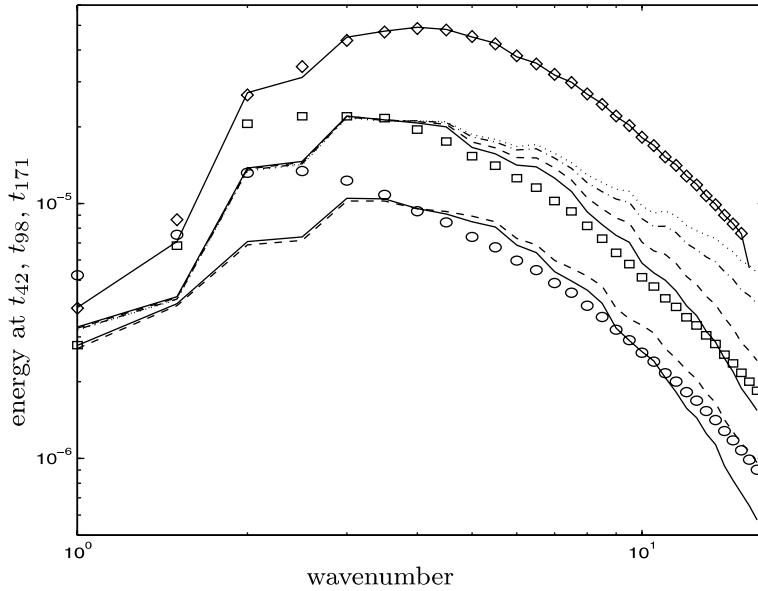


Fig. 6. Effect of the filter width ratio squared (α) on dynamic model results of isotropic turbulence. Simulations were performed with filter S1 on hexes. (\diamond): data at t_{42} ; (\square): data at t_{98} ; (\circ): data at t_{171} ; (—): initial condition matching the data; (---): simulation with $\alpha = 2$; (-.-): simulation with $\alpha = 3$; (-.-): simulation with $\alpha = 4$; (· · ·): simulation with $\alpha = 5$.

An analogous identity to that of Germano, this time between the $G_{\hat{\Delta}}$ -level and the $G_{\tilde{\Delta}}$ -level, leads to

$$Q_{ij} = \mathcal{F}_{ij} - \tilde{T}_{ij}, \tag{33}$$

which can be modeled through the Smagorinsky-type expressions in (7) and (26) and can be expressed through resolved quantities as

$$Q_{ij} = \tilde{u}_i \tilde{u}_j - \tilde{u}_i \tilde{u}_j \tag{34}$$

by using (22) and (23). Least squares minimization (with respect to $C_s^{\hat{\Delta}}$) of the difference between the modeled and resolved expressions for the deviatoric portion of Q_{ij} , leads to

$$(C_s^{\hat{\Delta}} \hat{\Delta})^2 = \frac{1}{2} \frac{\langle Q_{ij} N_{ij} \rangle}{\langle N_{kl} N_{kl} \rangle}, \tag{35}$$

where

$$N_{ij} = |\tilde{\mathcal{S}}| \tilde{\mathcal{S}}_{ij} - \gamma \vartheta |\tilde{\mathcal{S}}| \tilde{\mathcal{S}}_{ij}. \tag{36}$$

Here, $\gamma = (\tilde{\Delta}/\hat{\Delta})^2$ and $\vartheta = C_s^{\tilde{\Delta}}/C_s^{\hat{\Delta}}$. This seemingly introduces one more unknown in the form of $\xi_3 = \gamma \vartheta$ until we re-express it as

$$\gamma \vartheta = \left(\frac{\tilde{\Delta}}{\hat{\Delta}} \right)^2 \left(\frac{C_s^{\tilde{\Delta}}}{C_s^{\hat{\Delta}}} \right)^2 = \frac{(\tilde{\Delta}/\hat{\Delta})^2 (C_s^{\tilde{\Delta}}/C_s^{\hat{\Delta}})^2}{(\hat{\Delta}/\tilde{\Delta})^2 (C_s^{\hat{\Delta}}/C_s^{\tilde{\Delta}})^2} = \frac{\beta}{\alpha} \frac{\eta}{\zeta} = \frac{\xi_2}{\xi_1}. \tag{37}$$

Thus, $\xi_3 = \xi_2/\xi_1$. Letting the right hand side of (35) be defined as

$$\frac{1}{2} \frac{\langle Q_{ij} N_{ij} \rangle}{\langle N_{kl} N_{kl} \rangle} \equiv \Phi(\xi_2/\xi_1) \tag{38}$$

and dividing (35) by the expression in (24) (with $\xi_1 = \alpha\zeta$), we obtain

$$\xi_1 = \frac{\Phi(\xi_2/\xi_1)}{\Theta_1(\xi_1)}. \tag{39}$$

Thus, we have our second equation for the unknowns ξ_1 and ξ_2 . An alternate to the previous expression can be obtained by dividing (35) by (27) (with $\xi_2 = \beta\eta$) leading to

$$\xi_1 = \frac{\Phi(\xi_2/\xi_1)}{\Theta_2(\xi_2)}. \tag{40}$$

The expressions in (39) and (40) are equivalent as a consequence of (32).

Recently, in [16], a simplified version of (39) was derived under the assumption of scale-invariance, thus $\zeta = \eta = 1$ and $\xi_1 = \alpha$ and $\xi_2 = \beta$. In addition, the assumptions for α and β in (30) and (31) were made, resulting in a closed form of $\Phi(\xi_2/\xi_1)$ in the presence of well-characterized test filters whose widths are obtainable, such as those reviewed earlier. Scale-invariance and the assumptions in (30) and (31) amount to

$$\Phi(\xi_2/\xi_1) = \Phi(\beta/\alpha) = \Phi((\tilde{\Delta}/\hat{\Delta})^2). \tag{41}$$

Here the second equality is due to (30) and (31) which lead to

$$\frac{\beta}{\alpha} = \frac{(\tilde{\Delta}/\bar{\Delta})^2}{(\hat{\Delta}/\bar{\Delta})^2} = \frac{\kappa(\hat{\Delta}/h)^2}{\kappa(\tilde{\Delta}/h)^2} = \left(\frac{\hat{\Delta}}{\tilde{\Delta}}\right)^2 \tag{42}$$

a computable ratio given that test filters $G_{\tilde{\Delta}}$ and $G_{\hat{\Delta}}$ are explicitly applied and thus well-characterized. Under these simplifications, Eq. (39) has only one unknown, namely $\xi_1 = \alpha$, which after expansion of $\Theta_1(\xi_1)$ leads to a quadratic equation for ξ_1 . We refer to this simplified form as DFWR1. Thus, DFWR1 leads to dynamic estimation of the squared filter width ratio $\xi_1 = \alpha$ in the dynamic model in (10), as long as the test filter width ratio parameter (or the ratio between the widths of the well-characterized wide and standard test filters used), $\hat{\Delta}/\tilde{\Delta}$, can be obtained.

In what we refer to as DFWR2, we solve the full versions of the nonlinear algebraic coupled equations in (32) and (39) (without assumptions of scale-invariance nor assumptions in (30) and (31)) for the generalized filter width ratios $\xi_1 = \alpha\zeta$ and $\xi_2 = \beta\eta$ giving rise to a parameter-free, scale-dependent dynamic model in (24) or equivalently (27). The coupled nonlinear equations can be solved iteratively using Newton’s method as

$$\begin{bmatrix} \xi_1^{i+1} \\ \xi_2^{i+1} \end{bmatrix} = \begin{bmatrix} \xi_1^i \\ \xi_2^i \end{bmatrix} - \begin{bmatrix} \Theta_{,\xi_1}(\xi_1^i, \xi_2^i) & \Theta_{,\xi_2}(\xi_1^i, \xi_2^i) \\ \Psi_{,\xi_1}(\xi_1^i, \xi_2^i) & \Psi_{,\xi_2}(\xi_1^i, \xi_2^i) \end{bmatrix}^{-1} \begin{bmatrix} \Theta(\xi_1^i, \xi_2^i) \\ \Psi(\xi_1^i, \xi_2^i) \end{bmatrix}, \tag{43}$$

where

$$\Theta(\xi_1, \xi_2) \equiv \Theta_1(\xi_1) - \Theta_2(\xi_2) \tag{44}$$

and

$$\Psi(\xi_1, \xi_2) \equiv \xi_1 - \frac{\Phi(\xi_2/\xi_1)}{\Theta_1(\xi_1)}. \tag{45}$$

4. Numerical results: Decaying isotropic turbulence

In this section we present dynamic model results with DFWR2 and compare them with those of the dynamic model with DFWR1. We test DFWR2 on the decay of isotropic turbulence using the same hexahedral grid described earlier. In addition, we present results on tetrahedral and wedge grids. All grids contain 33 evenly spaced vertices in all three directions. The tetrahedral grid is obtained by splitting each hexahedral element into 6 tetrahedra and the wedge grid is obtained by splitting each hexahedral element into two wedges. For all the cases to be shown, the Newton iteration in (43) (required for DFWR2) converged to the same solution independent of the initial guess. First, in Fig. 7 we compare energy spectra obtained with DFWR1 and DFWR2 to experimental energy spectra data of [1] at non-dimensional time stations t_{98} and t_{171} . The energy spectrum of the initial condition in each simulation matching the experimental energy spectrum of [1] at t_{42} is shown as well. Figs. 8 and 9 show the temporal evolution of ξ_1 and the dynamic model coefficient. In the case of DFWR2, $\xi_1 = \alpha\zeta$ and the model coefficient is $(C_s^{\hat{\Delta}})^2$. In the case of DFWR1, $\xi_1 = \alpha$ and the model coefficient is $(C_s^{\hat{\Delta}})^2$. For DFWR2 and DFWR1, the energy spectra at t_{98} and t_{171} are similar and provide a good representation of the experimental data within the inertial range (i.e. wavenumbers between 3 and 8 in this case), as desired in an LES. Additionally, the temporal evolution of ξ_1 is roughly the same for DFWR1 and DFWR2 both using filters S1 and W1, leading to model coefficients which are very close to each other. Furthermore, this shows that for the current problem, the scale-invariance assumption in DFWR1 is not violated (i.e. $C_s^{\hat{\Delta}} \approx C_s^{\hat{\Delta}} \approx C_s^{\hat{\Delta}}$). In the case when both, DFWR1 and DFWR2, use filters S2 and W2, ξ_1 of DFWR2 is slightly higher than that of DFWR1. However, this slight difference hardly impacts the energy spectra for these two cases. In Figs. 10–12 we present results of the same problem but on the tetrahedral grid mentioned earlier. The results parallel those of the simulations performed on the hexahedral grid. Once again, energy spectra with DFWR2 and DFWR1 are very close to each other and accurate within the inertial range. Finally, Figs. 13–15 show results using the wedge grid

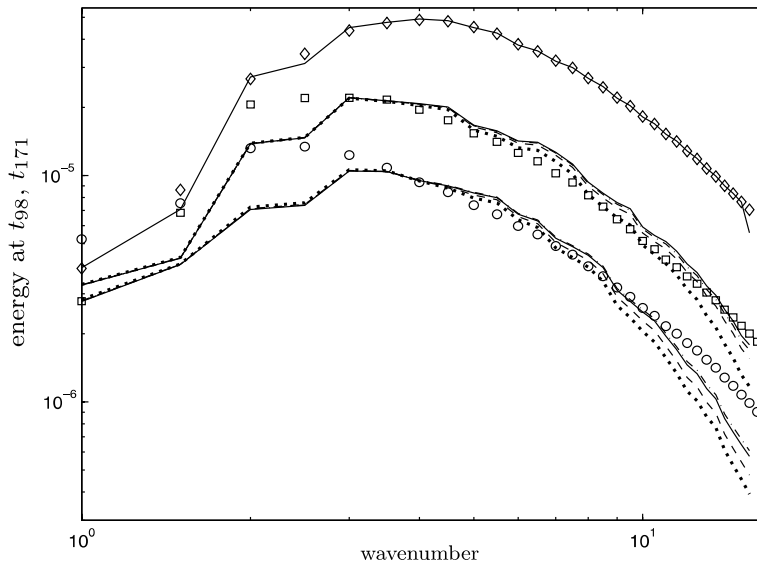


Fig. 7. Energy of the initial condition at t_{42} and energy at t_{98} and t_{171} after simulations with DFWR1 and DFWR2 on the hexahedral grid. (—): initial energy for all simulations; (—): DFWR2 with filters S1 and W1; (---): DFWR2 with S2 and W2; (---): DFWR1 with S1 and W1; (---): DFWR1 with S2 and W2; (\diamond): data at t_{42} ; (\square): data at t_{98} ; (\circ): data at t_{171} .

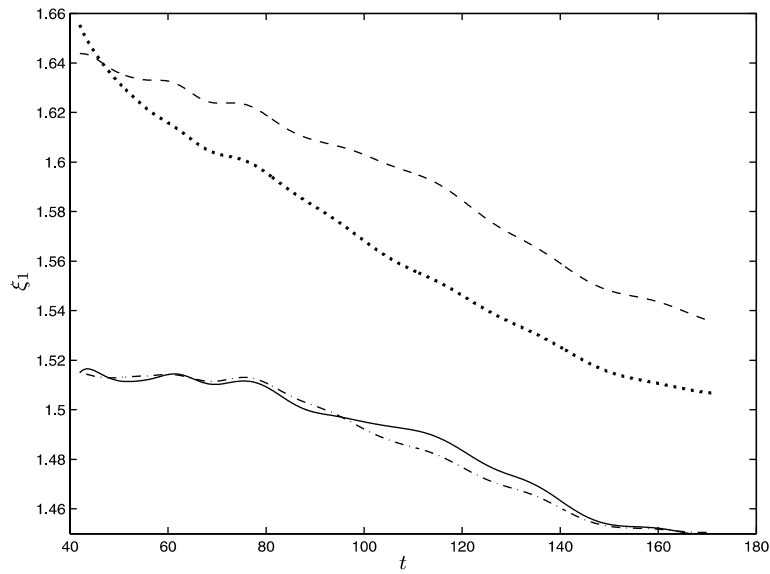


Fig. 8. Temporal evolution of ζ_1 , in the simulations on the hexahedral grid. (—): DFWR2 with filters S1 and W1; (---): DFWR2 with S2 and W2; (-·-): DFWR1 with S1 and W1; (···): DFWR1 with S2 and W2.

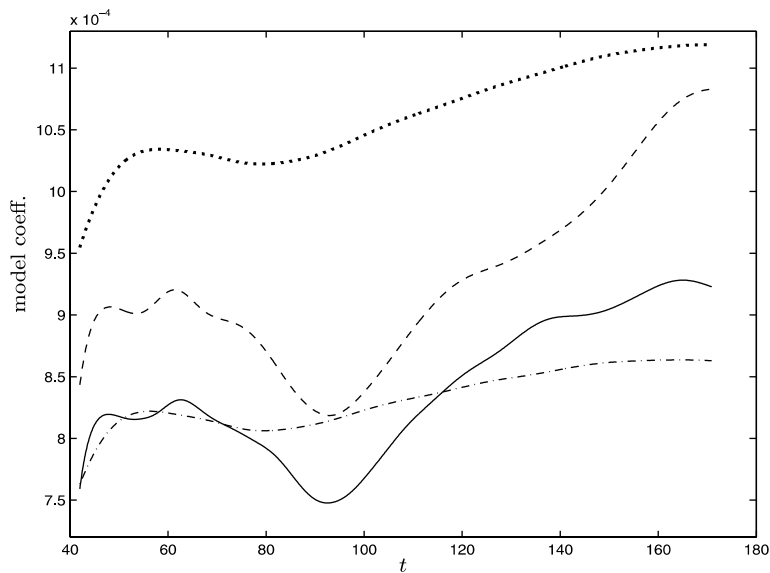


Fig. 9. Temporal evolution of dynamic model coefficient $((C_s^{\bar{\Delta}})^2$ for DFWR2 and $(C_s^{\bar{\Delta}})^2$ for DFWR1) in the simulations on the hexahedral grid. (—): DFWR2 with filters S1 and W1; (---): DFWR2 with S2 and W2; (-·-): DFWR1 with S1 and W1; (···): DFWR1 with S2 and W2.

mentioned earlier. In this case, nearly identical energy spectra are obtained with DFWR1 and DFWR2 using filters S2 and W2, as both represent well the energy spectra of the experimental data within the

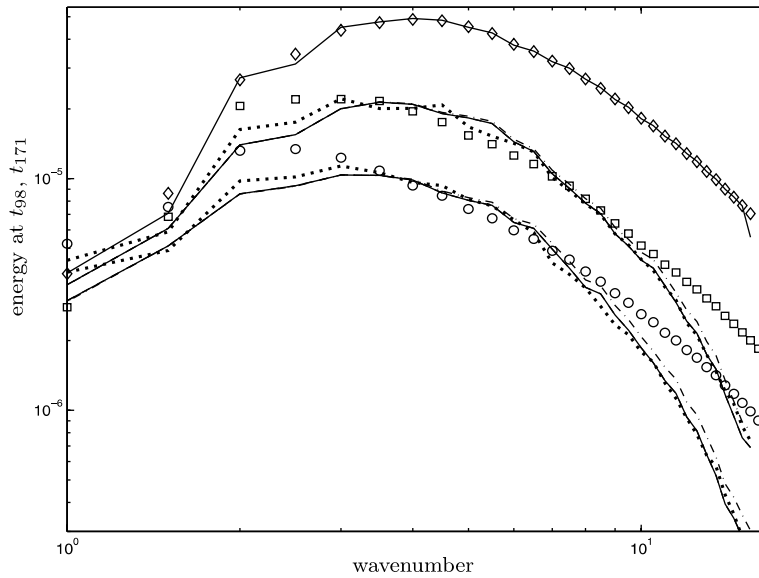


Fig. 10. Energy of the initial condition at t_{42} and energy at t_{98} and t_{171} after simulations with DFWR1 and DFWR2 on the tetrahedral grid. (—): initial energy for all simulations; (---): DFWR2 with filters S1 and W1; (-.-): DFWR2 with S2 and W2; (· · ·): DFWR1 with S1 and W1; (· · · ·): DFWR1 with S2 and W2; (\diamond): data at t_{42} ; (\square): data at t_{98} ; (\circ): data at t_{171} .

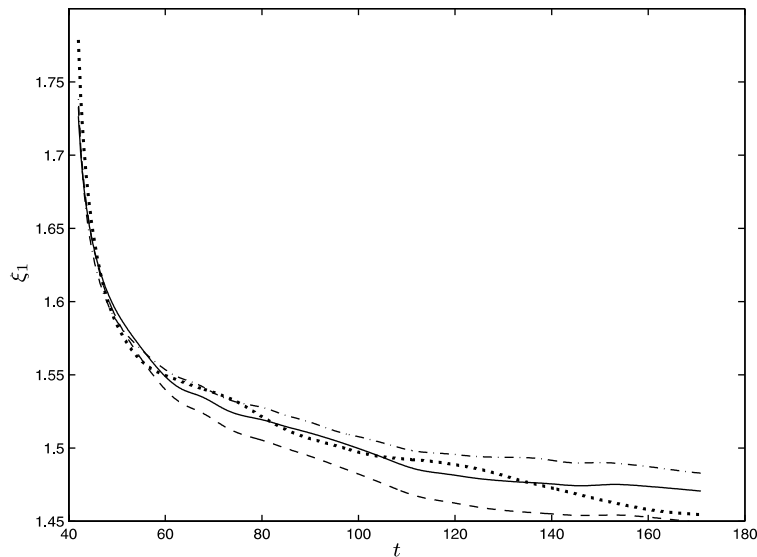


Fig. 11. Temporal evolution of ξ_1 in the simulations on the tetrahedral grid. (—): DFWR2 with filters S1 and W1; (---): DFWR2 with S2 and W2; (-.-): DFWR1 with S1 and W1; (· · ·): DFWR1 with S2 and W2.

inertial range. As can be seen from our results of decaying isotropic turbulence, the parameter-free dynamic model (DFWR2) performs just as well as its predecessor (DFWR1). In the case of DFWR1, knowledge of

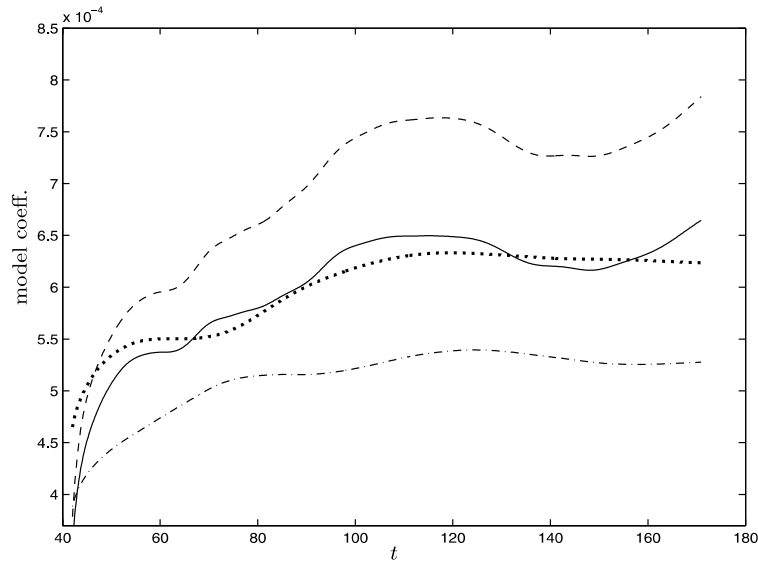


Fig. 12. Temporal evolution of the model coefficient in the simulations on the tetrahedral grid. (—): DFWR2 with filters S1 and W1; (---): DFWR2 with S2 and W2; (-.-): DFWR1 with S1 and W1; (....): DFWR1 with S2 and W2.

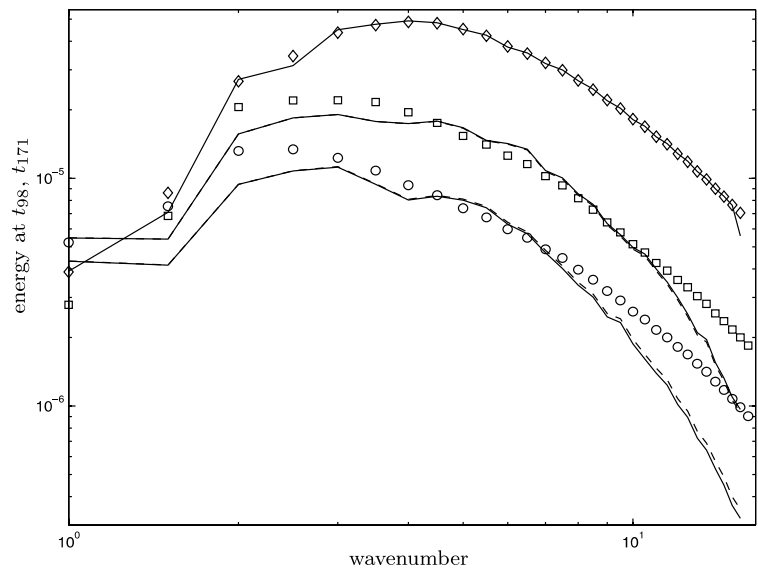


Fig. 13. Energy of the initial condition at t_{42} and energy at t_{98} and t_{171} after simulations with DFWR1 and DFWR2 on the wedge grid. (—): initial energy for all simulations; (—): DFWR2 with filters S2 and W2; (---): DFWR1 with S2 and W2; (O): data at t_{171} .

test filter transfer functions and widths are required for inputting the model parameter (i.e. the squared filter width ratios). In the self-contained DFWR2, tedious computations of test filter transfer functions and widths are not required.

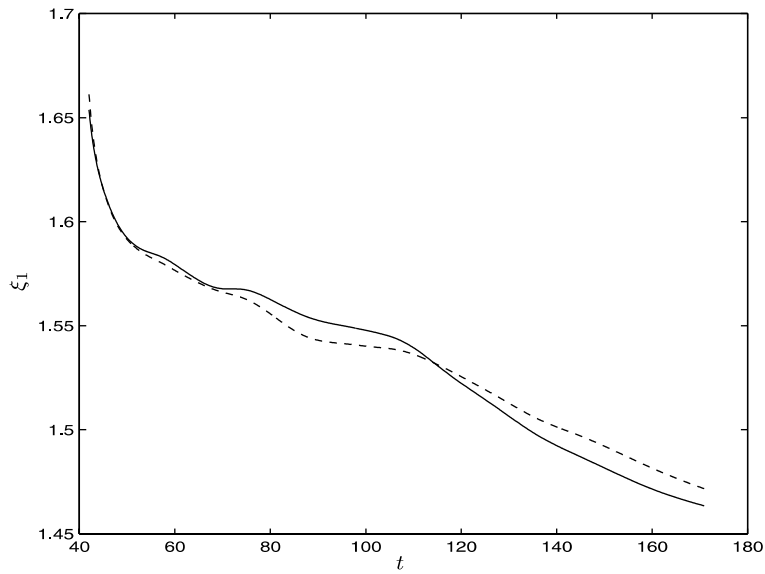


Fig. 14. Temporal evolution of ξ_1 in the simulations on the wedge grid. (—): DFWR2 with filters S2 and W2; (---): DFWR1 with S2 and W2.

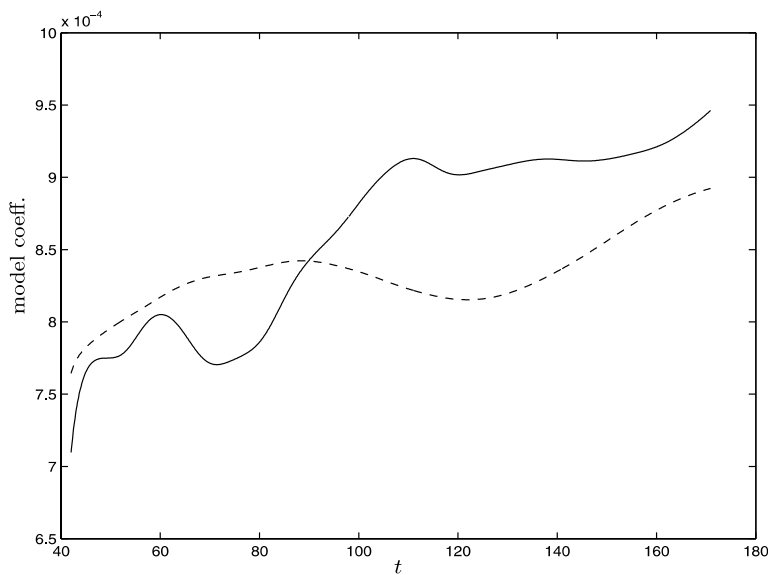


Fig. 15. Temporal evolution of the model coefficient in the simulations on the wedge grid. (—): DFWR2 with filters S1 and W1; (---): DFWR2 with S2 and W2; (-·-·): DFWR1 with S1 and W1; (·-·-·): DFWR1 with S2 and W2.

5. Conclusion

In this work we have derived and successfully tested a formulation for dynamic determination of the filter width ratio giving rise to a parameter-free dynamic model. Accurate determination of the filter width

ratio is of great importance as LES results may depend heavily on this parameter. Earlier models such as the classic dynamic model and DFWR1 relied on strong assumptions about the grid filter and on expensive computations to determine test filter widths. The new model obviates these difficulties by computing accurate values of the filter width ratio without the need to compute test filter widths. Such a model could be of great use in the future for large-eddy simulations on irregularly connected topologies for which test filter widths are even more difficult to obtain. The parameter-free model formulation incorporates ingredients used in an earlier effort ([16]) to determine the filter width ratio dynamically, namely Eq. (35) in addition to a new expression in (32). This last expression, which equates dynamic model coefficients computed with appropriate test filters, has been used in the past in the scale-dependent model of Porté-Angel et al. in [11]. Our motivation for using such expression is the important result that dynamic model coefficients computed with appropriate test filters can be roughly equal if the filter width ratio is computed consistently. Finally, the parameter-free model was derived without the use of scale-invariance, thus it could be considered scale-dependent. Here we have not tested this attribute of the model, however, we plan to do so in the near future. Furthermore, we also plan to test DFWR2 in wall-bounded flows.

Acknowledgements

This material is based upon work supported by the National Science Foundation under Grant No. 9985340. This work was also partially supported by the National Computational Science Alliance under Grant No. MCA01S014 and utilized the Origin2000 Array. We acknowledge Farzin Shakib of Acusim Software for the use of their linear equation solving libraries.

References

- [1] G. Comte-Bellot, S. Corrsin, Simple Eulerian time-correlation of full and narrow-band velocity signals in grid-generated 'isotropic' turbulence, *J. Fluid Mech.* 48 (1971) 273–337.
- [2] M. Germano, U. Piomelli, P. Moin, W.H. Cabot, A dynamic subgrid-scale eddy viscosity model, *Phys. Fluids A* 3 (1991) 1760–1765.
- [3] T.J.R. Hughes, L. Mazzei, K.E. Jansen, Large-eddy simulation and the variational multiscale method, *Comput. Visual. Sci.* 3 (2000) 47–59.
- [4] Thomas J.R. Hughes, *The Finite Element Method: Linear Static and Dynamic Finite Element Analysis*, Prentice Hall, Englewood Cliffs, NJ, 1987.
- [5] K.E. Jansen, A stabilized finite element method for computing turbulence, *Comput. Methods Appl. Mech. Engrg.* 174 (1999) 299–317.
- [6] D.K. Lilly, A proposed modification of the Germano subgrid-scale closure, *Phys. Fluids* 3 (1992) 2746–2757.
- [7] T.S. Lund, On the use of discrete filters for large-eddy simulation, in: *Annual Research Briefs*, Center for Turbulence Research, NASA Ames/Stanford University, 1997, pp. 83–95.
- [8] A.L. Marsden, O.V. Vasilyev, P. Moin, Construction of commutative filters for LES on unstructured meshes, *J. Comput. Phys.* 175 (2002) 584–603.
- [9] C. Meneveau, J. Katz, Scale-invariance and turbulence models for large-eddy simulation, *Annu. Rev. Fluid Mech.* 415 (2000) 1–32.
- [10] S.B. Pope, Large-eddy simulation using projection onto local basis functions, in: J.L. Lumley (Ed.), *Fluid Mechanics and the Environment: Dynamical Approaches*, Springer, 2000.
- [11] F. Porté-Angel, C. Meneveau, M.B. Parlange, A scale-dependent dynamic model for large-eddy simulation: application to the atmospheric boundary layer, *J. Fluid Mech.* 415 (2001) 261–284.
- [12] R.S. Rogallo, P. Moin, Numerical simulation of turbulent flows, *Annu. Rev. Fluid Mech.* 16 (1984) 99–137.
- [13] J. Smagorinsky, General circulation experiments with the primitive equations. I. The basic experiment, *Monthly Weather Rev.* 91 (1963) 99–152.
- [14] C.A. Taylor, T.J.R. Hughes, C.K. Zarins, Finite element modeling of blood flow in arteries, *Comput. Methods Appl. Mech. Engrg.* 158 (1998) 155–196.

- [15] A.E. Tejada-Martínez, K.E. Jansen, Spatial test filters for dynamic model large-eddy simulation on finite elements, *Commun. Numer. Methods Engrg.* 19 (2003) 205–213.
- [16] A.E. Tejada-Martínez, K.E. Jansen, A dynamic Smagorinsky model with dynamic determination of the filter width ratio, *Phys. Fluids* 16 (2004) 2514–2528.
- [17] O.V. Vasilyev, Computational constraints on large eddy simulation of inhomogeneous turbulent complex geometry flow, in: C. Liu, L. Sakell, T. Beutner (Eds.), *Proceedings of the Third AFOSR International Conference on DNS/LES*, Arlington, Texas, August 2001.
- [18] C.H. Whiting, K.E. Jansen, A stabilized finite element method for the incompressible Navier–Stokes equations using a hierarchical basis, *Int. J. Numer. Methods Fluids* 35 (2001) 93–116.
- [19] G.S. Winckelmans, A.A. Wray, O.V. Vasilyev, Testing of a new mixed model for LES: the Leonard model supplemented by a dynamic Smagorinsky term, in: *Proc. Summer Program VII (Center for Turbulence Research, Stanford, CA)*, Stanford University, 1998, pp. 367–387.